ANALYSIS OF TANDEM PROPELLERS INTERFERENCE WITH A HYBRID EULERIAN-LAGRANGIAN METHOD

Yi Yuan
Politecnico di Milano
Milan, Italy

Luigi Vigevano
Politecnico di Milano
Milan, Italy

ABSTRACT

A hybrid Eulerian–Lagrangian solver is applied to investigate aerodynamic interference in a tandem propeller configuration. The solver couples ROSITA with DUST to capture near-field loads and far-field wake structures efficiently. Grid convergence on a single three-blade propeller at advance ratio J=0.8 yields thrust and power coefficients within 1% and 3% of wind-tunnel measurements. For a tandem arrangement with axial spacing $L_a/R = 5$ and radial offset $L_r/R = 1$, the effects of phase offset and co/counter-rotation on the downstream propeller are quantified. In the baseline co-rotating case, the rear propeller incurs 7.4% thrust and 4.5% power losses and two-order-of-magnitude increases in unsteady fluctuations. Under the same rotational condition, a 30° phase offset magnify these losses and fluctuations, while 90° phase offset performs the opposite. Counter-rotation reduces oscillations by over 70% despite larger mean performance penalties. Blade-vortex interaction analysis reveals that phase control and rotation direction alter the alignment of tip vortices with the rear blade and thereby modify the induced velocities, governing loss and fluctuation characteristics.

NOTATION

*

Symbols

A Amplitude

c Chord, m

C_d Drag coefficient

C_l Lift coefficient

C_p Pressure coefficient

C_P Power coefficient

C_{M_z} Rotational momont coefficient

C_T Thrust coefficient

J Advance ratio

L_a, L_r Separation distance, m

M_t Tip Mach number

N Number of nodes

R Rotor radius, m

u_a Axial velocity, m/s

u_t Tangential velocity, m/s

V_∞ Freestream velocity, m/s

Δy_1 First layer thickness, m

η Propulsive efficiency

σ Standard deviation

ψ Azimuthal position

ω Vorticity magnitude

*

Acronyms

AOA Angle of Attack

BVI Blade-Vortex Interaction

CCW Counter Clock-Wise

CW Clock-Wise

DEP Distributed Electric Propulsion

eVTOL electric Vertical Take-Off and Landing

FMD Fused Deposition Modeling

NSCBC Navier-Stokes Characteristic Boundary Condition

PWM Pulse Width Modulation

RANS Reynolds-Averaged Navier–Stokes

ROSITA ROtorcraft Software ITAly

RPM Revolutions Per Minute

SA Spalart-Allmaras

SNG Spinner-Nacelle Grid

UAM Urban Air Mobility

VPM Vortex Particle Method

INTRODUCTION

In response to the increasing challenges of urban transportation and environmental sustainability, electric Vertical Take-Off and Landing (eVTOL) aircraft have gained significant attention as a transformative advancement for future Urban Air Mobility (UAM). Driven by Distributed Electric Propulsion (DEP), eVTOL configurations typically employ multiple closely-spaced rotors mounted on wings, booms, or fuselages. Such high rotor density enables compact layouts and redundancy but introduces complex aerodynamic interferences among rotors and lifting surfaces that can significantly degrade performance, increase noise, and complicate flight control. Understanding and mitigating these interferences is crucial for optimizing DEP configurations, therefore requiring precise simulations and experimental validations.

Indeed, multiple DEP systems has been proposed and the aerodynamic interferences within have been investigated experimentally (Refs. 1–3) and numerically in recent years. The latter have predominantly relied on Eulerian Reynolds-Averaged Navier–Stokes (RANS) solvers, which accurately capture viscous boundary layers and component loads (Refs. 4–6). However, to improve the accuracy of far-field vortex tracking due to inevitable numerical diffusion, high-fidelity schemes and considerable computational resources are often required (Ref. 7). Mid-fidelity Lagrangian solvers such as DUST (Refs. 8, 9) and FLOWUnsteady (Refs. 10, 11) have been employed to extend these databases, providing detailed wake visualizations yet lacking viscous near-body aerodynamic information.

Another alternative, the hybrid Eulerian-Lagrangian method (Refs. 12–14), which offers the advantage of accurately resolving aerodynamic loads while effectively preventing numerical dissipation of vortices with higher efficiency than Eulerian-based methods and higher accuracy than Lagrangian-based methods, has not been thoroughly explored for aerodynamic interference in such systems. The primary challenge to apply the hybrid method to a multi-rotor environment lies in coupling the induced velocity field and the vorticity carried by vortex particles with the Eulerian computational grids.

In this paper, we apply our recently developed hybrid Eulerian-Lagrangian solver (Ref. 14) to analyze a tandem propeller configuration, assessing different geometrical arrangements to give insights into the aerodynamic mechanisms of rotor-rotor interferences and evaluate the potential of hybrid solvers in accurately capturing interference effects with improved computational efficiency.

All simulations are performed on 64 cores of two AMD EPYC 7513 CPUs with speed of 2.60GHz on the high-performance cluster of Politecnico di Milano, CFDHub.

HYBRID EULERIAN-LAGRANGIAN SOLVER

The hybrid solver (Ref. 14) integrates a Eulerian solver ROSITA (Ref. 15) and a Lagrangian solver DUST (Ref. 16). The solver is designed to efficiently acquire a Eulerian-level accuracy of aerodynamic loads while maintaining the ability of capturing the farfield wake vortices with a Lagrangian approach. The two parental codes are briefly introduced below.

ROSITA solves unsteady RANS equations coupled with one-equation Spalart-Allmaras (SA) turbulence model (Ref. 17). The governing equations are discretized spatially using a Roe-MUSCL cell-centered finite volume approach (Ref. 18) and temporally a dual-time formulation (Ref. 19). In the hybrid scheme, the solver is only applied upon the near-body regions covered by structured grids, in the aim of interpreting the compressible and viscous flows around lifting bodies, such as propellers and wings.

On the other hand, DUST is a medium-fidelity open-source solver based on the integral boundary element method (BEM) and on the vortex particle method (VPM) (Ref. 20). Thanks to the approximation of discrete vorticity field and the Lagrangian convection-diffusion governing equation, it is capable of efficiently capturing and preserving the wake vorticity in a grid-free farfield (Refs. 8,21), which is essential for modeling blade-vortex interaction (BVI) in unconventional rotorcraft configurations.

The two solvers actively interact with each other at each time step such that from Eulerian to Lagrangian solver, the aerodynamic loads on the lifting bodies are extracted as a solution of RANS calculation and transformed into bound vortex strength of corresponding surface elements required by Lagrangian solver, following Kutta-Joukowsky theorem; from Lagrangian to Eulerian domain, the induced velocities from all the Lagrangian elements including surface elements and vortex particles correct the interface boundary condition of RANS grids, where Navior-Stokes Characteristic Boundary Condition (NSCBC) (Ref. 22) using ghost cells is adopted to ensure a bilateral non-reflection in regards of wake vortices.

The hybrid solver has been proved to achieve a more efficient computation of the rotor aerodynamics compared to a pure RANS method, as it only requires near-field grids while maintaining a less-diffusive wake in the farfield, against experimental data of several bechmark cases. Detailed formulation and validation of the hybrid solver can be found in our previous work (Ref. 14).

TANDEM PROPELLER TEST CASE

The propulsion unit employed in this work is a three-blade propeller with a spinner and a nacelle designed at Politecnico di Milano (Ref. 8) (hereinafter referred to as propeller). The blade is VarioProp 12C with a diameter of 300mm. The blades are mounted on a hub assembled with an aluminum spinner of 65 mm diameter, and a 270mm-length polycarbonate nacelle manufactured via Fused Deposition Modeling (FDM) technique completes the unit, as is shown in Figure 1(a). The propeller is driven by a Scorpion brushless motor and an external PWM-controlled electronic speed controller. It should be noted that the phase angles of propellers are not precisely controlled due to limitations of the hobby-grade components used.

In a tandem configuration, the two propellers are mounted perpendicular to the incoming flow, see Figure 1(b). The axial separation distance L_a/R is fixed at 5, a value chosen to emulate the inter-propeller row spacing of an Airbus Vahana-like eVTOL aircraft. The radial separation distance L_r/R can be varied from 0 to 2 to evaluate the aerodynamic interactions between the two propellers based on their degree of overlapping. Both propellers operated at a constant rotational speed of 7050 RPM, resulting in a tip Mach number (M_t) of 0.325 which is typical cruise speed of full-scale eVTOLs (Ref. 23). The propeller blades have a pitch angle of 26.5° at 75%R. The advancing speed of the tandem system spanned a range corresponding to moderate to fast cruise conditions (Refs. 24, 25), specifically from a free-stream velocity V_∞ of 14.1 m/s (advance ratio $J = 0.4$) to 35.2 m/s (advance ratio $J = 1.0$). The experimental campaign is conducted at the S.De Ponte wind tunnel of Politecnico di Milano.

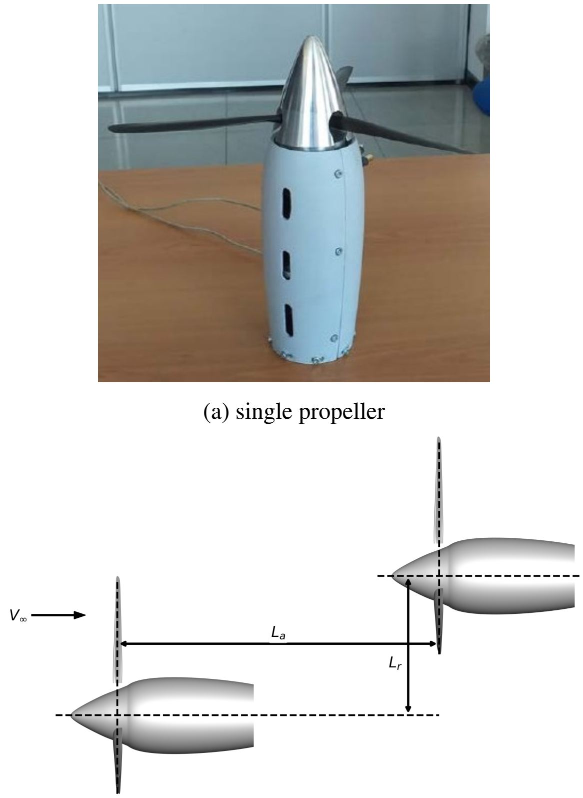

(a) single propeller

(b) layout of tandem models

Figure 1: The configuration of tandem propellers

RESULTS AND DISCUSSION

Single Propeller Performance

A preliminary verification on a single propeller at an advance ratio of $J = 0.8$ is carried out to assess the accuracy of current hybrid solver since the propeller's blade are geometrically different from the the conventional helicopter ones in terms of the spanwise twist, aspect ratio and kinematic control. After rebuilding the blade geometry by 3D scanning, three O-block body-fitted grids with different spatial resolutions are generated, namely Coarse, Medium and Fine, and the grid information is reported in Table 1. To avoid complexity of the rotating parts, the spinner and nacelle are regarded as a fixed integrated unit (SNG), and a body-fitted grid of 0.85M nodes is generated accordingly. For the purpose of comparing the computational result with pure RANS solution, a Cartesian near-field with a maximum grid spacing of 0.02R and a Cartesian far-field background grid are supplied. The CHIMERA overset grid system and a close look at Medium grid of the blade surface is shown in Figure 2.

Table 1: Single propeller: body-fitted blade grid information(i: chordwise, j: spanwise, k: normal, Δy_1: first layer thickness)

Grid	N_{tot}	$N_{i,j,k}$	$\Delta y_1 \times 10^5$
Coarse	0.76M	$136 \times 82 \times 44$	6.67R
Medium	1.22M	$141 \times 141 \times 126$	3.33R
Fine	1.69M	$208 \times 95 \times 54$	1.67R

The simulation was firstly performed using ROSITA without SNG to assess the grid sensitivity of the blades. Table 2 reports the propeller's thrust coefficient C_T, power coefficient C_P and propulsive efficiency η computed by different grids. Compared to the experiment result, the C_T differences of Coarse, Medium, Fine girds are 5.7%, 1.0% and 1.0% respectively, implying that Medium grid meets the requirements for grid independence. However, it is observed that the ROSITA solver tends to overpredict C_P, showing an error of 2.7% with the Medium grid, consequently leading to a 3.9% underestimation of the propulsive efficiency.

Table 3 presents the propeller performance results at $J = 0.8$ from various methods. Unlike the Eulerian ROSITA solver, the hybrid solver overpredicts by 2.0% compared to experiment, and C_P is overpredicted by 6.5%. The inclusion of SNG in the ROSITA simulation results in a minor reduction in C_T

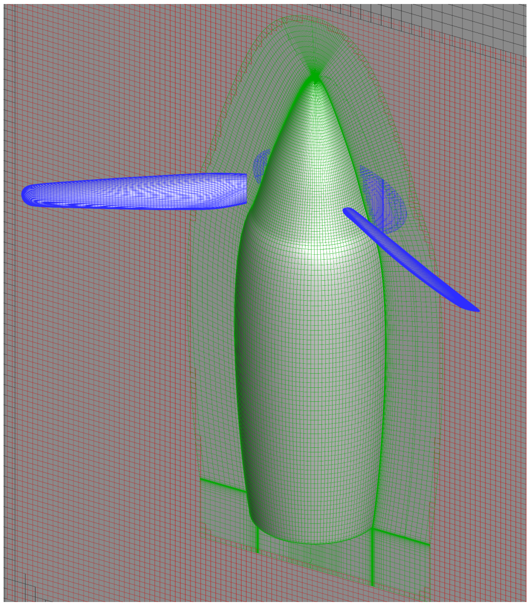

(a) Overset grid

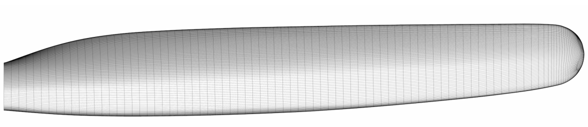

(b) Blade surface grid

Figure 2: Single propeller: grid system and blade grid

Table 2: Single propeller: grid independence study of thrust coefficient C_T, power coefficient C_P and propulsive efficiency η

Grid	C_T	C_P	η
Exp	0.101	0.107	0.755
Coarse	0.095	0.105	0.723
Medium	0.100	0.110	0.726
Fine	0.100	0.110	0.726

while the power coefficient C_P remains consistent.

The results align with Caccia et al's (Ref. 26) and Zanotti et al's (Ref. 8) work, which is also listed in the table. It appears that the Eulerian-based solvers (ROSITA, SU2) tend to under-predict C_T but overpredict C_P, whereas Lagrangian-based solver (DUST) overpredicts both of them. The observed errors are attributable to model accuracy, discrepancies in operational conditions, and the specific numerical schemes employed. Nevertheless, the hybrid solver, with its blade-only model, reproduces the propeller's performance with sufficient accuracy and is capable of investigating the tandem configuration.

Tandem Propeller Performance

On the basis of the prior single-propeller computation, the tandem propeller configuration is simulated and analyzed. The radial distance L_r/R of the two propeller is fixed to 1, as is confirmed (Ref. 8) that in this condition the rear propeller experiences the the most fluctuations and unsteadiness. Moreover, the impact of rotational direction and phase control are considered, in which the phase control is realized by offsetting the starting azimuth angle of the rear propeller to 30°, 60° and 90° in terms of its rotational direction. The complete settings of operating conditions with their shortened abbreviations is reported in Table 4.

Method	SNG	C_T	C_P	η
Experiment	–	0.101	0.107	0.755
ROSITA	w/o	0.100	0.110	0.726
ROSITA	w/	0.098	0.110	0.707
Hybrid	w/o	0.103	0.114	0.722
DUST (Ref. 8)	w/	0.112	0.114	0.786
DUST (Ref. 26)	w/	0.106	0.113	0.750
SU2 (Ref. 26)	w/	0.097	0.111	0.699

Table 3: Single propeller: thrust, power coefficients and propulsive efficiency of the propeller at $J = 0.8$ using different methods compared with experiment

Table 4: Tandem propeller: complete settings of operation condition

Case	rotational direction		Phase offset	
	Front	Rear	Front	Rear
CW-CW_0	CW	CW	0°	0°
CW-CW_30	CW	CW	0°	30°
CW-CW_60	CW	CW	0°	60°
CW-CW_90	CW	CW	0°	90°
CW-CCW_0	CW	CCW	0°	0°
CW-CCW_30	CW	CCW	0°	30°
CW-CCW_60	CW	CCW	0°	60°
CW-CCW_90	CW	CCW	0°	90°

CW-CW_0 serves as the baseline configuration in this work, as it undergoes both experiments (not synchronized) and simulation with DUST (Ref. 8). Table 5 presents the performance, associated losses, and standard deviations for both the front and rear propellers, processed from the last revolution. The losses and standard deviation increments are defined as

$$\Delta C_{T,P} = \left(\frac{C_{T,P}^{\text{front,rear}}}{C_{T,P}^{\text{single}}} - 1 \right) \times 100\% \tag{1}$$

$$\Delta \sigma_{C_{T,P}} = \frac{\sigma_{T,P}^{\text{front,rear}}}{\sigma_{T,P}^{\text{single}}} - 1 \tag{2}$$

Under this specific configuration, the front propeller exhibits less than 0.1% variation in both C_T and C_P, a negligible change that aligns with experimental observations. The reduction of performance of the rear propeller is somewhat more relevant than that of the front propeller, yet remaining within few percent. From the data reported in Table 6, it may be observed that the present predictions are closer to the experimental values than those of DUST (Ref. 8).

Based on the standard deviation of C_T and C_P, the dynamic fluctuation of the performance of front propeller is limitedly

Table 5: Tandem propeller: performance, its losses and standard deviation increment of front and rear propellers for case CW-CW_0 at $J = 0.8$ (negative denotes losses and positive denotes gains)

Propeller	C_T	ΔC_T	$\Delta\sigma_{C_T}$	C_P	ΔC_P	$\Delta\sigma_{C_P}$
Front	0.103	+0.04%	2.98	0.114	+0.10%	4.92
Rear	0.096	-7.44%	156	0.109	-4.45%	226

Table 6: Rear propeller: performance losses compared with experimental and DUST results for case CW-CW_0 at $J = 0.8$ (negative denotes losses and positive denotes gains)

Method	ΔC_T	ΔC_P
Exp (Ref. 8)	-4.7%	-3.6%
DUST (Ref. 8)	-9.8%	-6.7%
Hybrid	-7.44%	-4.45%

amplified, while those of rear propeller are escalated by hundreds of times, becoming a non-negligible source of aeroacoustic noise, mechanical vibration and fatigue. Since the blade phase angle was not synchronized during the experiment, the experimental values of the amplitudes of critical frequencies are not precise. However, $3/rev$, $6/rev$ are highlighting frequencies of the tandem configuration (Ref. 8), of which $6/rev$ reaches maximum value when $L_r/R = 1$, becoming one of the major contributions to the fluctuation of C_T and C_P. Therefore, Table 7 gives the quantitative data of the major spectrum for a single propeller, and Table 8 reports the magnification factor of these two frequencies for both front and rear propellers as a comparison for the rest of the simulation, which is define similar to $\Delta\sigma_{C_{T,P}}$ as

$$\Delta A_{C_T} = \frac{A_{T,P}^{\text{front,rear}}}{A_{T,P}^{\text{single}}} - 1 \tag{3}$$

The results indicate that the values of the amplitude of $6/rev$ are approximately half of $3/rev$'s for the single propeller's C_T and C_P. Under CW-CW_0 tandem configuration, the amplitudes of front propeller are increased at a minimal level, whereas those of rear propeller are magnified substantially. Since the value of the $3/rev$ component is greater than that of the $6/rev$ component, the former is the major impact on the performance fluctuation. Moreover, the following analysis will only address the performance of rear propeller.

Table 7: Single propeller: amplitude of major frequencies in performance spectrum at $J = 0.8$

Propeller	$A_{C_T}(3)$	$A_{C_T}(6)$	$A_{C_P}(3)$	$A_{C_P}(6)$
Single	1.21E-5	6.33E-6	6.44E-6	3.00E-6

Table 9 present the performance and its losses and standard deviation increments of the rear propeller, at the operating conditions of Table 4, with respect to the baseline case CW-CW_0. The relative losses and relative standard deviation increments are defined as

Table 8: Tandem propeller: amplitude increase of major frequencies in performance spectrum of front and rear propellers for case CW-CW_0 at $J = 0.8$

Propeller	$\Delta A_{C_T}(3)$	$\Delta A_{C_T}(6)$	$\Delta A_{C_P}(3)$	$\Delta A_{C_P}(6)$
Front	3.23	2.99	3.15	5.87
Rear	589	291	563	510

$$\Delta C_{T,P}^{*} = \frac{\Delta C_{T,P}^{\text{rear}}}{\Delta C_{T,P}^{\text{CW-CW\_0,rear}}} \tag{4}$$

$$\Delta\sigma_{C_{T,P}}^{*} = \frac{\Delta\sigma_{T,P}^{\text{rear}}}{\Delta\sigma_{T,P}^{\text{CW-CW\_0,rear}}} \tag{5}$$

Note that a larger $\Delta C_{T,P}^{*}$ means an increase in the losses and reversely a lower $C_{T,P}$. The differences in mean C_Ts and C_Ps between the co-rotating and counter-rotating cases become evident. Generally, the front propeller's impact on the overall performance of the counter-rotating rear propeller is larger, resulting in averaged relative losses of 34% for C_T and 52% for C_P respectively, while the fluctuation is noticeably reduced. Considering the large absolute magnitude of the fluctuations, it can be inferred that counter-rotating configurations can improve the rear propeller's aerodynamically induced oscillations of the aerodynamic coefficients. For instance, comparing CW-CW_30, which exhibits the largest standard deviation, with CW-CCW_30, which has the smallest, the fluctuations can be relatively reduced by more than 62% for C_T and 66% for C_P.

Table 10 list the variations of the amplitudes of major components within the performance fluctuation for rear propeller. Similarly, the relative variations of the amplitudes are calculated as

$$\Delta A_{T,P}^{*} = \frac{\Delta A_{C_{T,P}}^{\text{rear}}}{\Delta A_{C_{T,P}}^{\text{CW-CW\_0,rear}}} \tag{6}$$

In co-rotating rear configurations, with the exception of the CW-CW_30 case (which exhibits the largest standard deviation), phase control has a very limited impact on the $6/rev$ amplitude while effectively reducing the $3/rev$ frequency amplitude. In contrast, the CW-CW_30 case leads to a mild raise in the $3/rev$ amplitude but a significant drop in the $6/rev$ amplitude. However, as analyzed above, the amplitude of the $3/rev$ frequency primarily contributes to the propeller performance fluctuation. Consequently, the fluctuation in the CW-CW_30 case increases, while it decreases in other co-rotating cases. For counter-rotating configurations, drawing parallels with the co-rotating analysis, the CW-CCW_30 case displays the smallest $3/rev$ frequency amplitude, thus resulting in the

Table 9: Tandem propeller: performance, its losses and standard deviation increment of rear propellers at $J = 0.8$ normalized by case CW-CW_0

Case	C_T	ΔC_T^*	$\Delta \sigma_{C_T}^*$	C_P	ΔC_P^*	$\Delta \sigma_{C_P}^*$
CW-CW_0	0.0955	1.0	1.0	0.109	1.0	1.0
CW-CW_30	0.0942	1.17	1.17	0.108	1.30	1.25
CW-CW_60	0.0950	1.07	0.973	0.109	1.11	0.975
CW-CW_90	0.0956	0.987	0.738	0.110	0.939	0.716
CW-CCW_0	0.0932	1.31	0.763	0.107	1.48	0.725
CW-CCW_30	0.0934	1.28	0.438	0.107	1.41	0.426
CW-CCW_60	0.0925	1.39	0.675	0.106	1.58	0.590
CW-CCW_90	0.0926	1.38	0.798	0.106	1.59	0.714

lowest fluctuation. Reversely, although the CW-CCW_90 case has the smallest $6/rev$ amplitude, its $3/rev$ frequency amplitude is the largest, leading to the highest fluctuation.

Further examination reveals that the performance losses and standard deviation (or $3/rev$ amplitude) increments do not necessarily introduce a linear relationship. Figure 3 and Figure 4 compares the C_T and C_P contribution of a single blade of the rear propeller as a function of its azimuth angle with respect to the radial offset direction. All the curves present two local minimums around $\psi = 140°$ and 230, denoting entering and exiting the overlapping region of the blade, while the loads recover around $\psi = 180°$ when the blade is temporarily far from the wake vortices of the front propeller. The differences among the cases are the values of the local minimums and maximums. For co-rotating cases, the most fluctuated configuration CW-CW_30 has the lowest sum of local minimums and the least fluctuated CW-CW_90 has the largest, implying strongest and weakest total interactions respectively. However, although CW-CCW_30 and CW-CCW_90 still hold the lowest and largest minimum summations, their performance fluctuation is reversed. This is attributed to the superposition of three blades loads with 120° phase offset, as the time histories of C_T and C_P of the last revolution shown in Figure 5 and Figure 6. Note that the performance losses of counter-rotating cases are larger because the load recovery around $\psi = 180°$ is less significant. As a result, the overall performance and spectrum analysis do not fully reflect the real oscillation condition of the blades.

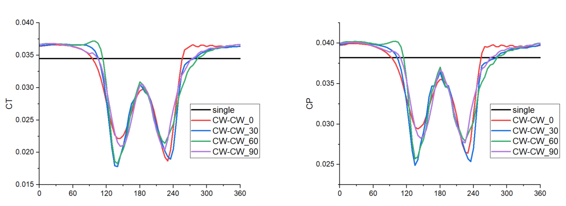

(a) C_T (b) C_P

Figure 3: Rear propeller: load contribution of a single blade as a function of its azimuth angle with respect to the radial offset direction for co-rotating cases at $J = 0.8$

The following analysis tries to provide more details on the

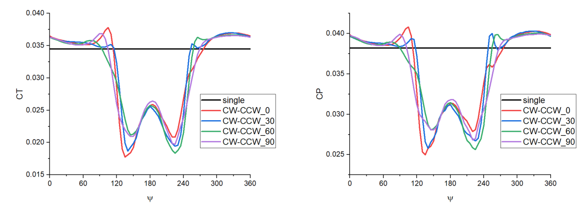

(a) C_T (b) C_P

Figure 4: Rear propeller: load contribution of a single blade as a function of its azimuth angle with respect to the radial offset direction for counter-rotating cases at $J = 0.8$

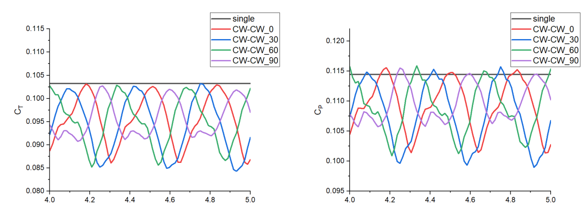

(a) C_T (b) C_P

Figure 5: Rear propeller: load time histories of the last revolution for co-rotating cases at $J = 0.8$

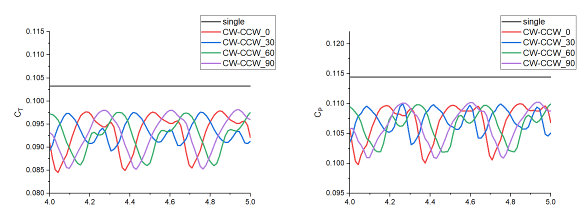

(a) C_T (b) C_P

Figure 6: Rear propeller: load time histories of the last revolution for counter-rotating cases at $J = 0.8$

cases where the rear propeller exhibits the strongest and weakest overall fluctuations within both co-rotating and counter-rotating propeller configurations as aforementioned. For the CW-CW configuration, the polar distributions of ΔC_l, ΔC_d and ΔC_{M_z}, $\Delta u_a/V_\infty$, $\Delta u_t/V_\infty$ and ΔAoA, which are the variations with respect to the single propeller simulation, are shown in Figures 7-10. It is important to note that for the hybrid

Table 10: Tandem propeller: amplitude increase of major frequencies in performance spectrum of rear propeller at $J = 0.8$ normalized by case CW-CW_0

Case	$\Delta A^*_{C_T}(3)$	$\Delta A^*_{C_T}(6)$	$\Delta A^*_{C_P}(3)$	$\Delta A^*_{C_P}(6)$
CW-CW_0	1.0	1.0	1.0	1.0
CW-CW_30	1.22	0.307	1.30	0.351
CW-CW_60	0.970	1.04	0.965	1.14
CW-CW_90	0.715	1.00	0.674	1.11
CW-CCW_0	0.707	1.26	0.638	1.36
CW-CCW_30	0.354	1.04	0.163	1.35
CW-CCW_60	0.652	0.940	0.535	0.191
CW-CCW_90	0.820	0.465	0.733	0.0970

solver, the velocity at collocation points of lifting line elements does not directly influence the aerodynamic loads on the blade. Therefore, the variations of u_a, u_t and AOA are only used as a diagnostic tool for examination.

Starting from a phase angle of 30°, the rear propeller blade likely encounters the most intense and coherent regions of the front propeller's wake during rotation. As is presented in Figure 8, when the blade enters the overlappping region, the $\Delta u_a/V_\infty$ contour shows a evidently negative stripe while there is also a less obvious but still negative stripe when the blade exits. Concurrently, $\Delta u_t/V_\infty$ is also increased significantly at both of these two moments. The variations of the two velocities result in a highly oscillatory effective AOA, consequently causing notable fluctuations in the distributed performance parameters (ΔC_l, ΔC_d and ΔC_{M_z}) at the respective position.

Conversely, a starting phase angle of 90° allows the rear propeller blade circumvent the most detrimental regions of the wake from the front propeller. The wake's influence on the blade's aerodynamic performance becomes more diffused and balanced, as demonstrated in Figure 10 (a) and (b) where the two stripes with extreme velocities fade. This leads to reduced unfavorable interference and, and consequently relatively smaller thrust and power losses.

The situation becomes rather different under counter-rotating configuration. Since the rear propeller rotates in the opposite direction to the front propeller, it aligns with the swirl component of the front propeller's slipstream. Hence, the effective tangential velocity u_t on the rear propeller blade, induced by the front propeller's slipstream, is generally smaller compared to a co-rotating setup. This effect is visually observed in Figure 12(b) and Figure 14(b), where the magnitudes of $\Delta u_t/V_\infty$ tend to be slightly but not obviously larger compared to co-rotating cases, as well in Figure 3 and Figure 4, where the load recovery of counter-rotating propellers is reduced. Due to this interaction, the rear propeller in counter-rotating configurations experiences slightly lower C_T and C_P compared to co-rotating ones.

From the fluctuation perspective, the diagnostic $\Delta u_a/V_\infty$ and $\Delta u_t/V_\infty$ contours in Figure 12 and Figure 14 exhibit opposite extreme value stripes in the blade entry and exit regions. Regarding the Effective AoA, compared to co-rotating configurations, the two regions where AoA decrease are connected at the blade root given that the lowest rotational speed of blades encounters the highest swirl velocities generated by the front propeller's blade tips. For CW-CCW_30 case, the distribution of these two regions extends from blade root to tip, causing more apparent losses in outboard area, whereas the losses are more concentrated at the root for CW-CCW_90 case.

As a conclusive remark at this stage, the hybrid solver proves its effectiveness for predicting the performance of complex tandem propeller configurations. Moreover, when phase control is feasible, this technique can be employed to reduce thrust losses that impact overall performance and to mitigate its fluctuations. Regarding the choice of rotational direction, an optimal solution could be selected by making a trade-off between fluctuations and thrust losses. It should also be noted that the performance fluctuation is not necessarily positively correlated with load fluctuations on the blade.

Tandem Propeller Flowfield Analysis

A more in-depth study on the aerodynamic interaction between the wake from front propeller and the rear propeller is provided based on both the Lagrangian and Eulerian flow field in this section. Rather than using cases with extreme fluctuations of overall performance, the investigation centers on the local interactive effect between blade and vortex, thus the selected cases are CW-CW_30, CW-CCW_0 and CW-CCW_60.

Coarse BVI processes within different cases are described briefly according to the evolution of tip wake and blade position post-proceed from Lagrangian field solution in the following figures, where the vortices are extracted by Q-criterion = 0.1 and colored by vorticity magnitude. The target blades are distinguished with pressure distribution C_p.

Figure 15 presents the BVI process as the target blade enters the overlapping region for the CW-CW_30 case. The spiral tip vortices generated by the front propeller are inclined to the target blade and mostly remain beneath it. Furthermore, the blade cuts off these vortices from the outer side of their arc. The region on the blade affected by these vortices extends from approximately $0.6R$ towards outboard to the blade tip. Additionally, during the roll-up process, the tip vortices generated by the target blade also interact and subsequently merge with the developed tip vortex from the front propeller.

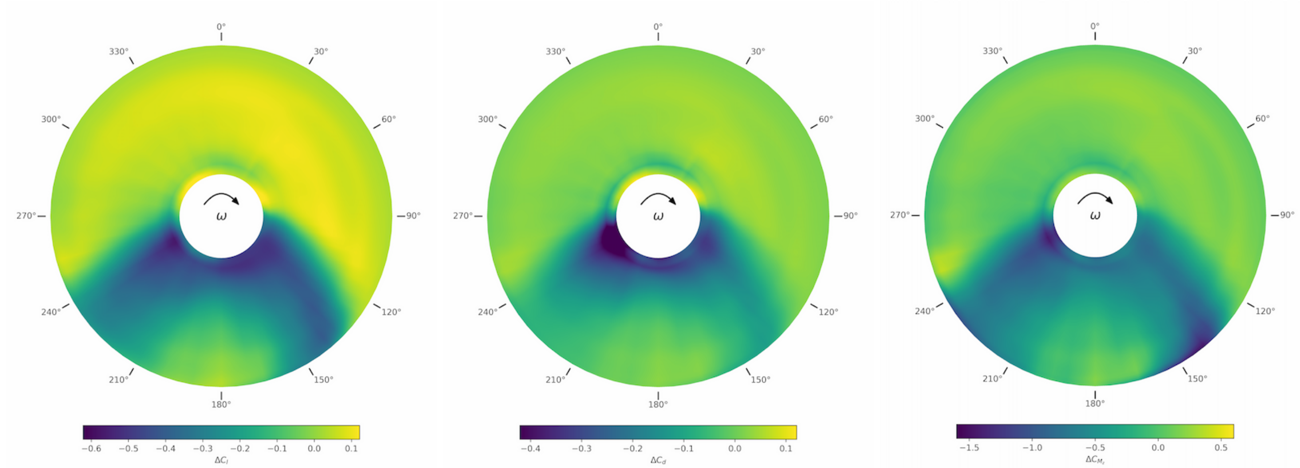

(a) ΔC_l (b) ΔC_d (c) ΔC_{M_z}

Figure 7: Rear propeller: Eulerian lift, drag and axial moment coefficients on the disk plane for case CW-CW_30 at $J = 0.8$

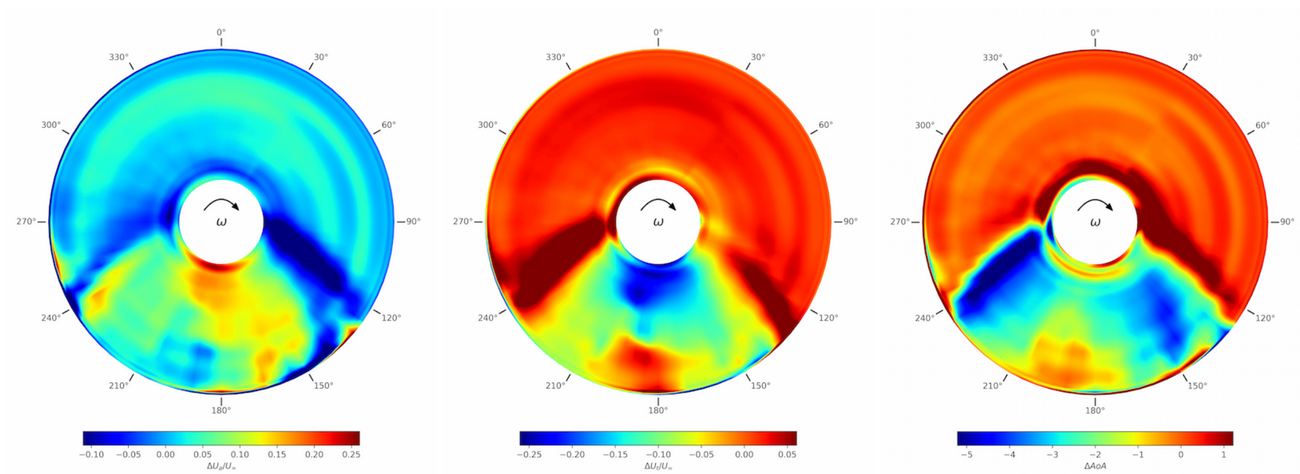

(a) $\Delta u_a/V_\infty$ (b) $\Delta u_t/V_\infty$ (c) Effective ΔAoA

Figure 8: Rear propeller: Lagrangian axial and tangential velocities and effective angle of attack on the disk plane for case CW-CW_30 at $J = 0.8$

The broken vortices are reconnected since their directions of vorticity form an acute angle in space.

As the target blade exits the overlapping region (Figure 16), the blade intercepts the arc of the tip vortices from its inner side. The inclination and position of the tip vortices relative to the blade are mirrored compared to the entry process, and consequently, the affected region on the blade transitions inwards from tip. The vortex-vortex interaction is also observed.

The BVI process of blade entering the overlapping region in CW-CCW_0 case (Figure 17) and exiting in CW-CCW_60 cases (Figure 18) are also presented as the tip vortices intersect with the mid-blade and have the most significant impact on a large portion of the span. In Figure 17, the inclined tip vortice pipe encounters the blade at approximately $0.6R$. For the inboard blade section, the vortices are located above the blade's suction surface, while for the outboard blade section, the vortices are positioned below the blade's pressure surface. The developed vortices are cut-off and remain separated since $\psi = 110°$, and the vortices near the pressure side of blade are slightly relocated towards the direction of blade motion. On the other hand, the oblique BVI in Figure 18 is reversed, where the blade cuts off the developed vortices from its inner side of arc, and the vortices stays above the outboard of the blade and under the inboard of the blade. According to the variation of blade load of one revolution in Figure 4, the BVI intensity of entering the overlapping region in CW-CCW_0 case is somewhat stronger than exiting in CW-CCW_60 case.

It is worth noting that the azimuthal angle at which a clear visual interaction occurs between the blade and the vortex does not correspond to the local minimum blade loading shown in Figure 3 and Figure 4. When entering the overlapping region, the degradation in loading shows a certain delay, whereas during the exiting phase, the recovery of loading occurs earlier, probably due to the unsteady effect of the inter-propeller in-

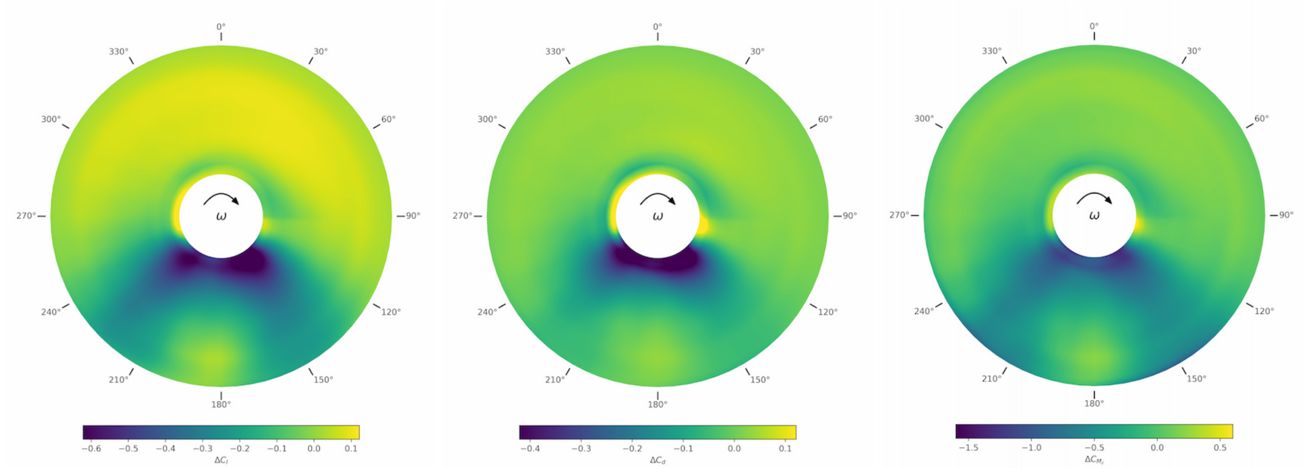

(a) ΔC_l (b) ΔC_d (c) ΔC_{M_z}

Figure 9: Rear propeller: Eulerian lift, drag and axial moment coefficients on the disk plane for case CW-CW_90 at $J = 0.8$

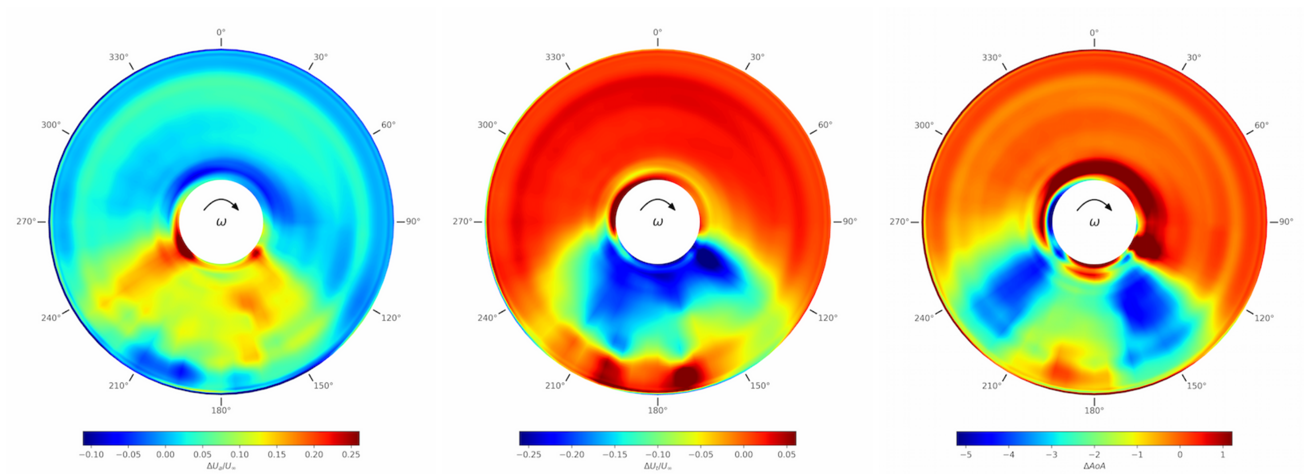

(a) $\Delta u_a/V_\infty$ (b) $\Delta u_t/V_\infty$ (c) Effective ΔAoA

Figure 10: Rear propeller: Lagrangian axial and tangential velocities and effective angle of attack on the disk plane for case CW-CW_90 at $J = 0.8$

teraction.

A finer evaluation is performed within the five sections ($0.35R$, $0.5R$, $0.65R$, $0.80R$ and $0.95R$) of RANS grids at critical azimuth angle of aerodynamic interactions in terms of non-dimensional spanwise vorticity and normalized chordwise velocity. Figure 19 corresponds to blade entering overlapping region at $\psi = 125°$ for CW-CW_30 case. The outboard-pointing tip vortices are captured at the leading edge of the $0.95R$ section. At the suction side of this section, the negative vorticity layer thickens, and the positive chordwise velocity region is suppressed, indicating boundary layer thickening. At other sections, an additional layer with positive spanwise vorticity emerges on the suction side, and the positive chordwise velocity regions shrink. An extra secondary vortex is observed shedding from the leading edge. The reverse flow region near the trailing edge extends towards the downstream.

In Figure 20, the blade is exiting the overlapping region at $\psi = 240°$ for CW-CW_30. A vortex trajectory with negative spanwise vorticity is observed across sections from $0.95R$ to $0.50R$, and it intersects the blade's leading edge at the tip. The positive chordwise velocity region is stretched towards the propeller's advancing direction, while its overall magnitude decreases, similar to that observed during the entering phase.

Figure 21 and Figure 22 present vortices with contrast direction pass through the RANS grid in different inclination for the contra-rotating cases. The vortices collide with the blade at intermediate section $0.50R$ and $0.65R$. However, since the vortex direction is opposite to the vorticity stemming from velocity gradiant of the suction surface, as is shown in Figure 22(b), the chordwise flows are indeed accelerated. The same condition complies with the pressure side at section $0.35R$ and $0.50R$, where a notable positive chordwise region

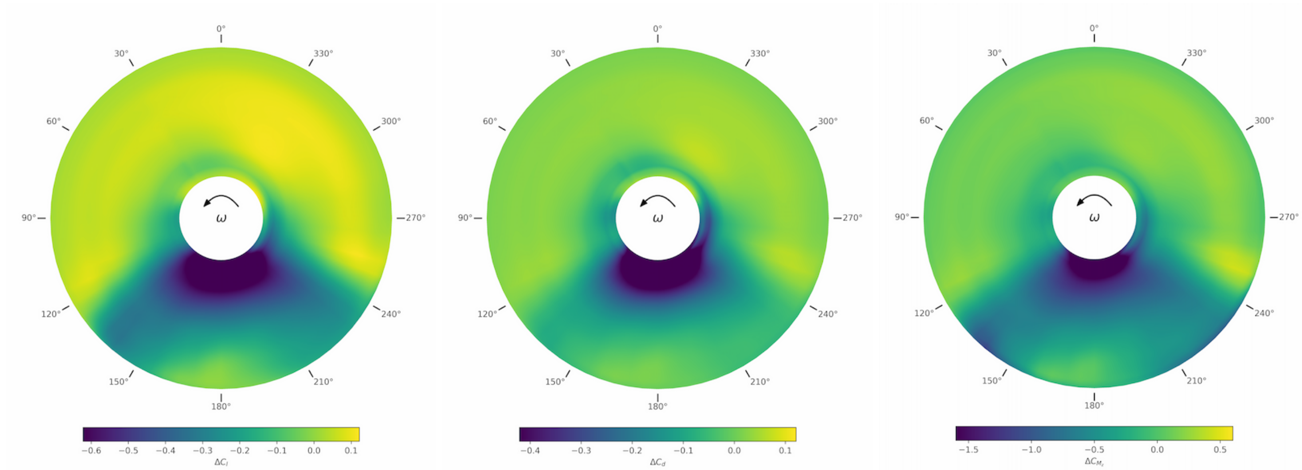

(a) ΔC_l (b) ΔC_d (c) ΔC_{M_z}

Figure 11: Rear propeller: Eulerian lift, drag and axial moment coefficients on the disk plane for case CW-CCW_30 at $J = 0.8$

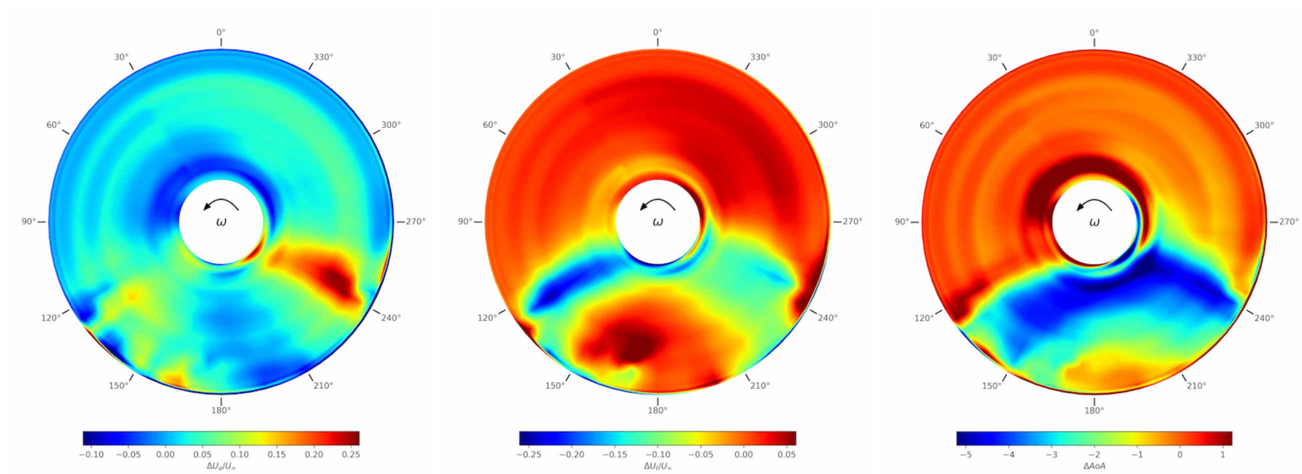

(a) $\Delta u_a/V_\infty$ (b) $\Delta u_t/V_\infty$ (c) Effective ΔAoA

Figure 12: Rear propeller: Lagrangian axial and tangential velocities and effective angle of attack on the disk plane for case CW-CCW_30 at $J = 0.8$

emerges. On the order hand, aligned vortices distort the flows around the blade section, making the interaction even more severe, which is also demonstrated for the suction side in Figure 19.

CONCLUSIONS

In this work, the hybrid Eulerian-Lagrangian solver is applied on a tandem configuration of propellers, emphasizing effects of the phase control and rotational direction on the rear propeller. Main conclusions are as follows:

1. The hybrid Eulerian-Lagrangian solver accurately predicts single propeller performance at cruise advance ratio $J = 0.8$, matching experimental thrust and power within 1% and 3%. In the baseline co-rotating tandem case (CW-CW_0), the rear propeller suffers a 7.4% thrust and 4.5% power loss, with unsteady fluctuations increasing by two orders of magnitude, while the front propeller remains nearly unaffected. The results agree well with DUST results.

2. Phase control and co/counter-rotation play a critical role in the rear propeller's overall performance. Under co-rotating configuration, a 30° phase offset in co-rotation leads to blades encountering tip vortices, increasing thrust/power losses and oscillations, whereas a 90° offset avoids vortices. Counter-rotation reverses the inflow swirl velocity for the rear propeller, causing more loading losses but greatly lowering the fluctuations.

3. BVI analysis shows the unsteady load changes correspond to rear blade entry and exit through the slipstream with tip vortices from front propeller. Phase control and co/counter-rotating configuration adjust the relative alignment of the tip vortices and the rear blade, altering

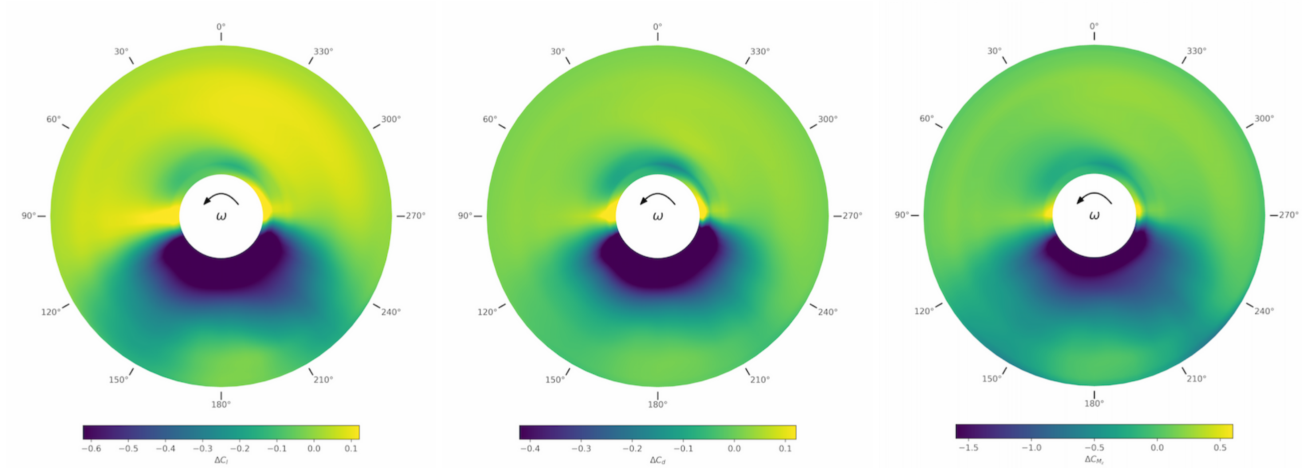

(a) ΔC_l (b) ΔC_d (c) ΔC_{M_z}

Figure 13: Rear propeller: Eulerian lift, drag and axial moment coefficients on the disk plane for case CW-CCW_90 at $J = 0.8$

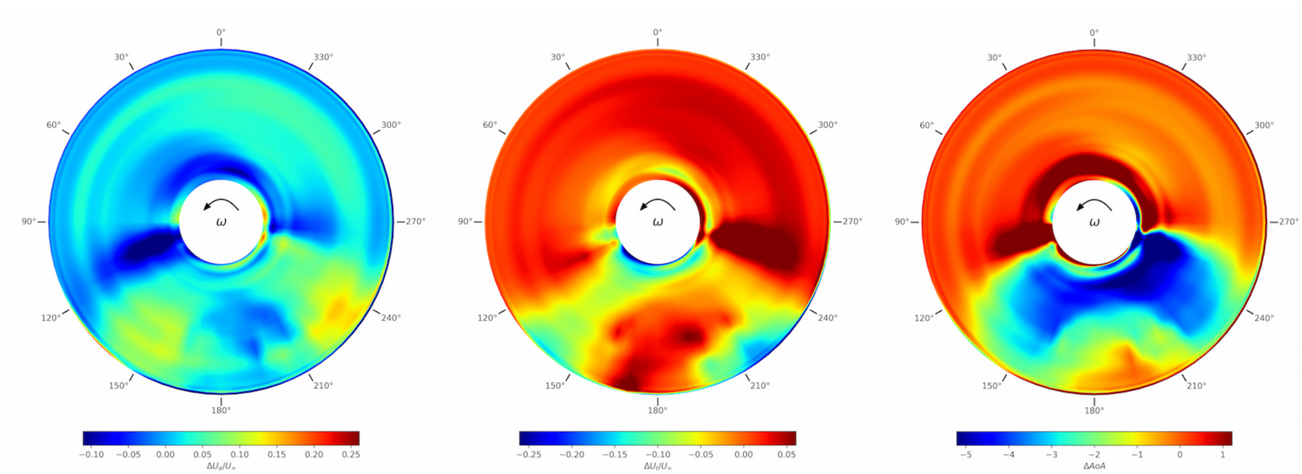

(a) $\Delta u_a/V_\infty$ (b) $\Delta u_t/V_\infty$ (c) Effective ΔAoA

Figure 14: Rear propeller: Lagrangian axial and tangential velocities and effective angle of attack on the disk plane for case CW-CCW_90 at $J = 0.8$

spanwise variations in induced chordwise velocity and thus interaction severity.

Author contact: Yi Yuan yi.yuan@polimi.it Luigi Vigevano luigi.vigevano@polimi.it

ACKNOWLEDGMENTS

The authors acknowledge the computational resource of the high performance cluster CFD-Hub at Politecnico di Milano. The author Yi Yuan would like to thank the China Scholarship Council for financial support under the Grant No. 202006250025.

REFERENCES

1. Brazinskas, M., Prior, S. D., and Scanlan, J. P., "An Empirical Study of Overlapping Rotor Interference for a Small Unmanned Aircraft Propulsion System," *Aerospace*, Vol. 3, (4), December 2016, pp. 32. DOI: 10.3390/aerospace3040032.

2. Droandi, G., Zanotti, A., Gibertini, G., Grassi, D., and Campanardi, G., "Experimental Investigation of the Rotor-Wing Aerodynamic Interaction in a Tiltwing Aircraft in Hover," *The Aeronautical Journal*, Vol. 119, (1215), May 2015, pp. 591–612. DOI: 10.1017/S0001924000010708.

3. Zhu, H., Du, Y., Nie, H., Xin, Z., and Geng, X., "Experimental Investigation of Aerodynamic Interaction in Non-Parallel Tandem Dual-Rotor Systems for Tiltrotor UAV," *Drones*, Vol. 9, (5), May 2025, pp. 374. DOI: 10.3390/drones9050374.

4. Wang, K., Zhou, Z., Zhu, X., and Xu, X., "Aerodynamic Design of Multi-Propeller/Wing Integra-

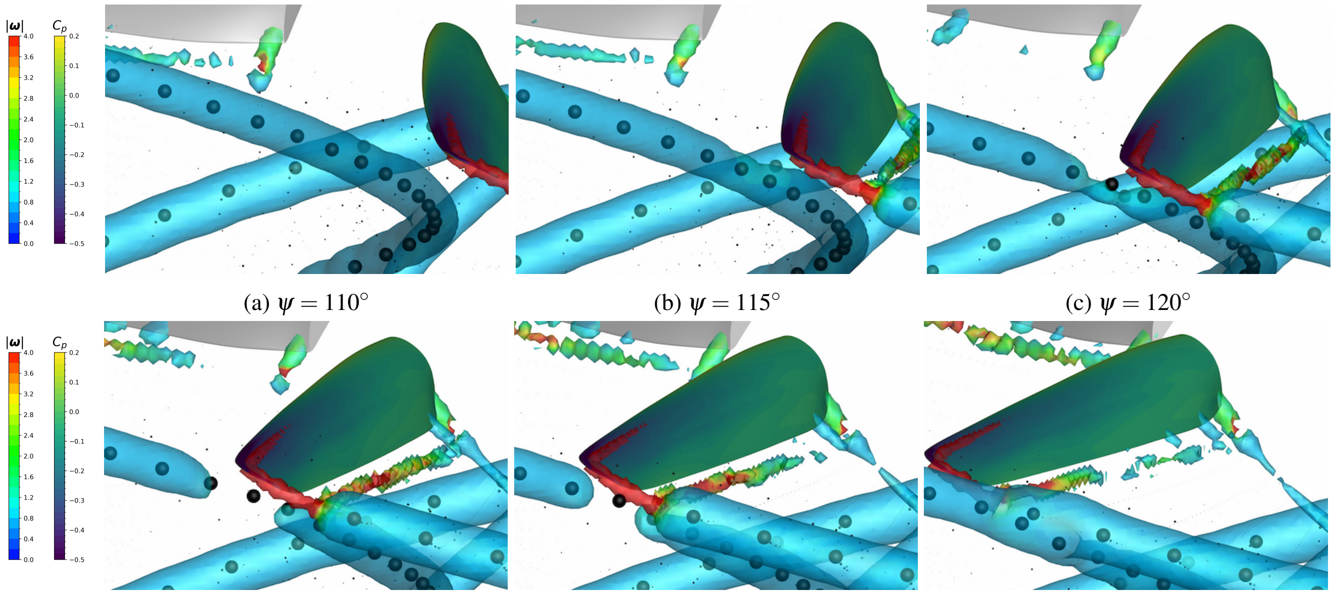

(a) $\psi = 110°$ (b) $\psi = 115°$ (c) $\psi = 120°$

(d) $\psi = 125°$ (e) $\psi = 130°$ (f) $\psi = 135°$

Figure 15: Rear propeller: BVI process when blade enters overlapping region for case CW-CW_30 at $J = 0.8$

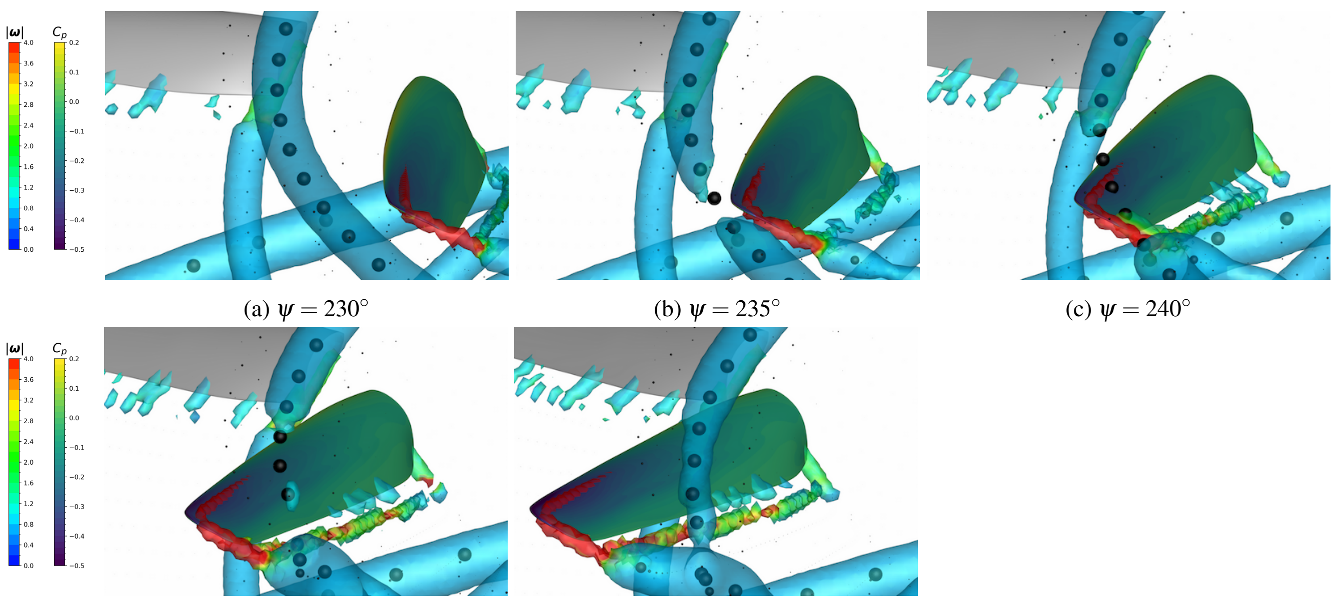

(a) $\psi = 230°$ (b) $\psi = 235°$ (c) $\psi = 240°$

(d) $\psi = 245°$ (e) $\psi = 250°$

Figure 16: Rear propeller: BVI process when blade exits overlapping region for case CW-CW_30 at $J = 0.8$

tion at Low Reynolds Numbers," *Aerospace Science and Technology*, Vol. 84, January 2019, pp. 1–17. DOI: 10.1016/j.ast.2018.07.023.

5. Healy, R., Misiorowski, M., and Gandhi, F., "A CFD-Based Examination of Rotor-Rotor Separation Effects on Interactional Aerodynamics for eVTOL Aircraft," *Journal of the American Helicopter Society*, Vol. 67, (1), January 2022, pp. 1–12. DOI: 10.4050/JAHS.67.012006.

6. Qiao, G., Zhang, T., and Barakos, G. N., "Numerical Simulation of Distributed Propulsion Systems Using CFD," *Aerospace Science and Technology*, Vol. 147, April 2024, pp. 109011. DOI: 10.1016/j.ast.2024.109011.

7. Yoon, S., Lee, H. C., and Pulliam, T. H., "Computational Study of Flow Interactions in Coaxial Rotors," AHS Technical Meeting on Aeromechanics Design for Vertical Lift, 2016.

8. Zanotti, A., and Algarotti, D., "Aerodynamic Interaction Between Tandem Overlapping Propellers in eV-

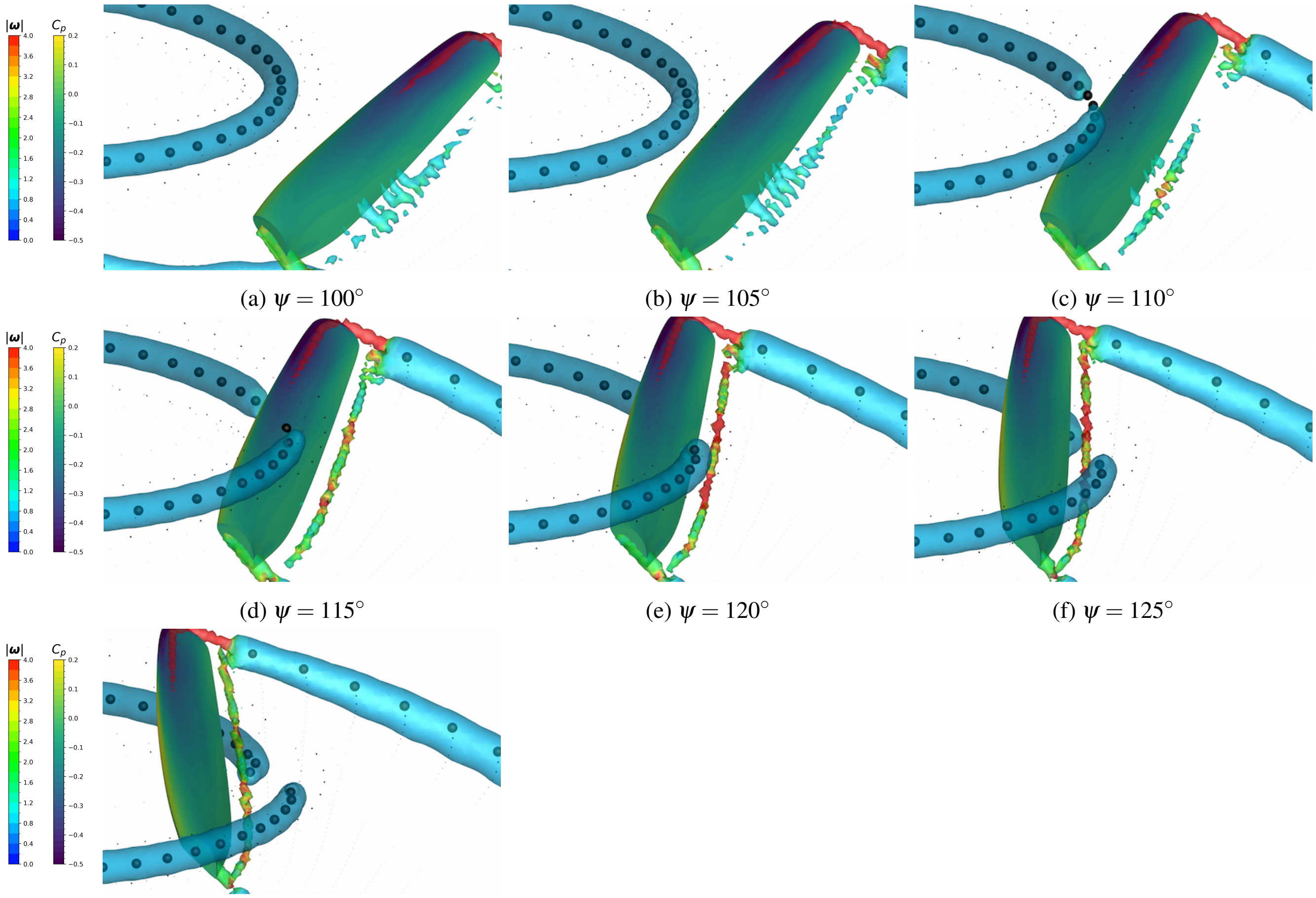

(a) $\psi = 100°$ (b) $\psi = 105°$ (c) $\psi = 110°$

(d) $\psi = 115°$ (e) $\psi = 120°$ (f) $\psi = 125°$

(g) $\psi = 130°$

Figure 17: Rear propeller: BVI process when blade enters overlapping region for case CW-CCW_0 at $J = 0.8$

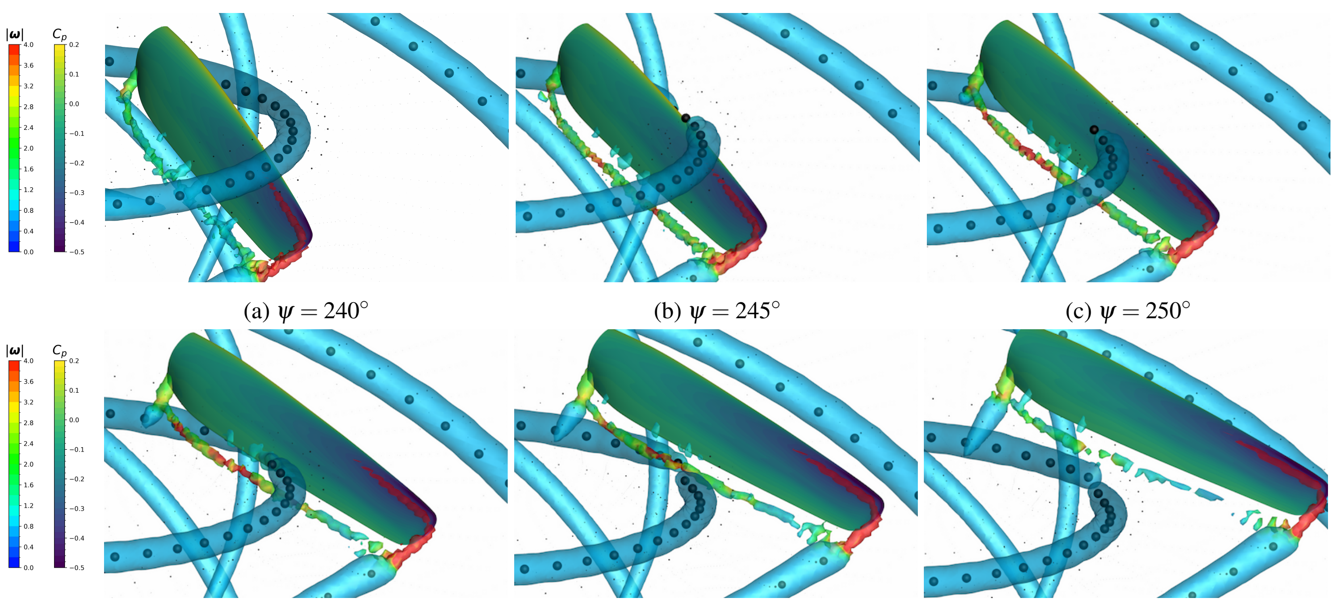

(a) $\psi = 240°$ (b) $\psi = 245°$ (c) $\psi = 250°$

(d) $\psi = 255°$ (e) $\psi = 260°$ (f) $\psi = 265°$

Figure 18: Rear propeller: BVI process when blade exits overlapping region for case CW-CCW_60 at $J = 0.8$

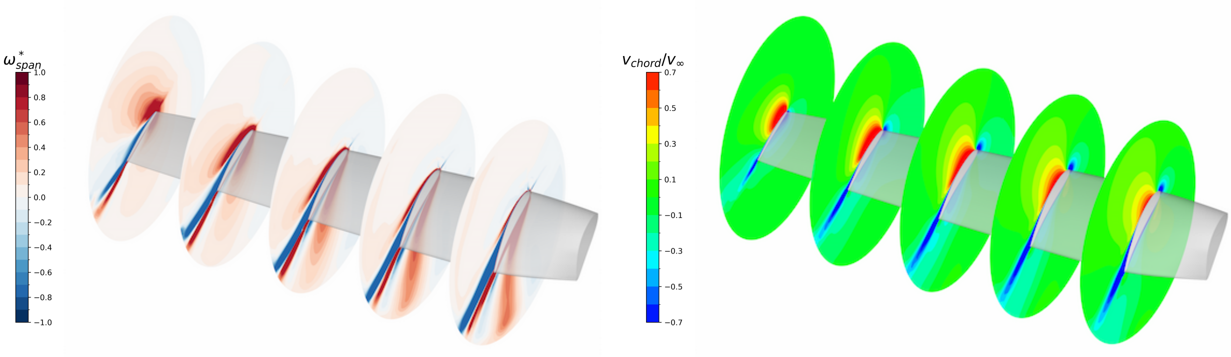

(a) non-dimensional spanwise vorticity

(b) normalized chordwise relative velocity

Figure 19: Rear propeller: BVI when blade enters overlapping region at $\psi = 125°$ for case CW-CW_30 at $J = 0.8$

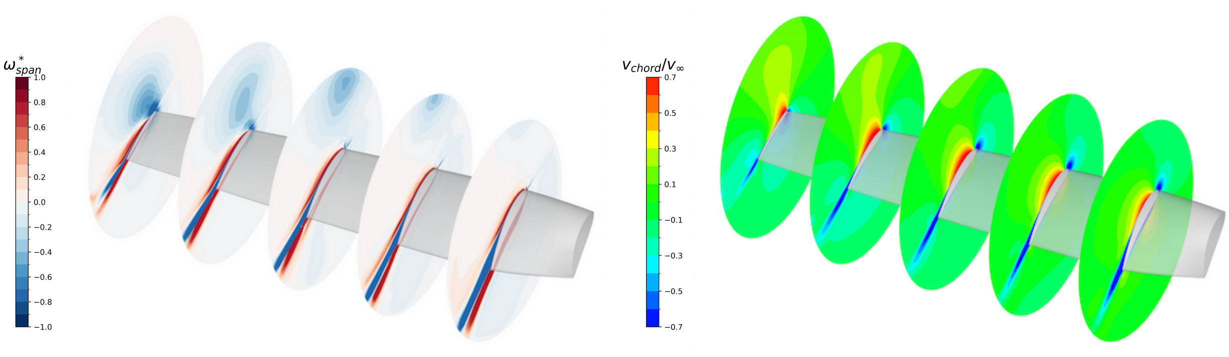

(a) non-dimensional spanwise vorticity

(b) normalized chordwise relative velocity

Figure 20: Rear propeller: BVI when blade exits overlapping region at $\psi = 240°$ for case CW-CW_30 at $J = 0.8$

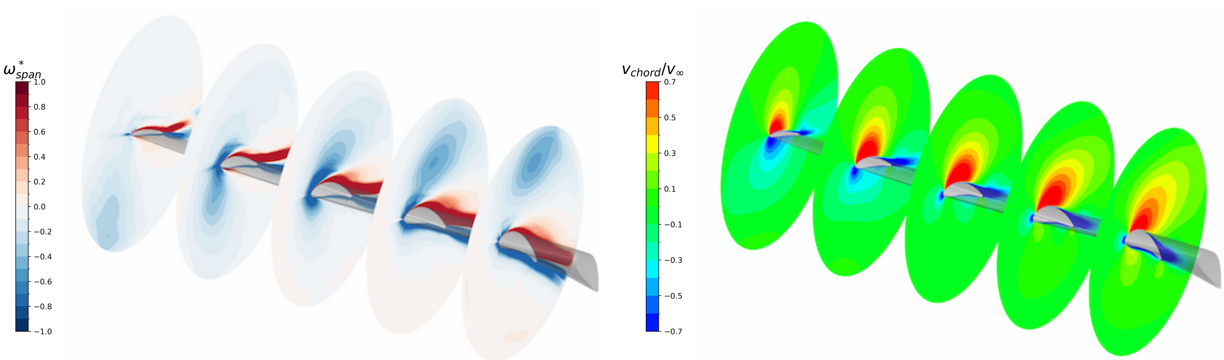

(a) non-dimensional spanwise vorticity

(b) normalized chordwise relative velocity

Figure 21: Rear propeller: BVI when blade enters overlapping region at $\psi = 115°$ for case CW-CCW_0 at $J = 0.8$

TOL Airplane Mode Flight Condition," *Aerospace Science and Technology*, Vol. 124, May 2022, pp. 107518. DOI: 10.1016/j.ast.2022.107518.

9. Niro, C., Savino, A., Cocco, A., and Zanotti, A., "Mid-Fidelity Numerical Approach for the Investigation of Wing-Propeller Aerodynamic Interaction," *Aerospace Science and Technology*, Vol. 146, March 2024, pp. 108950. DOI: 10.1016/j.ast.2024.108950.

10. Alvarez, E. J., Mehr, J., and Ning, A., "FLOWUnsteady: An Interactional Aerodynamics Solver for Multirotor Aircraft and Wind Energy," AIAA AVIATION 2022 Forum, 2022. DOI: 10.2514/6.2022-3218.

11. Alvarez, E. J., and Ning, A., "Meshless Large-Eddy Simulation of Propeller–Wing Interactions with Reformulated Vortex Particle Method," *Journal of Aircraft*, Vol. 61, (3), May 2024. DOI: 10.2514/1.C037279.

12. Moushegian, A. M., and Smith, M. J., "Dual-Solver Hybrid Computational Approach to Integrated Propulsion

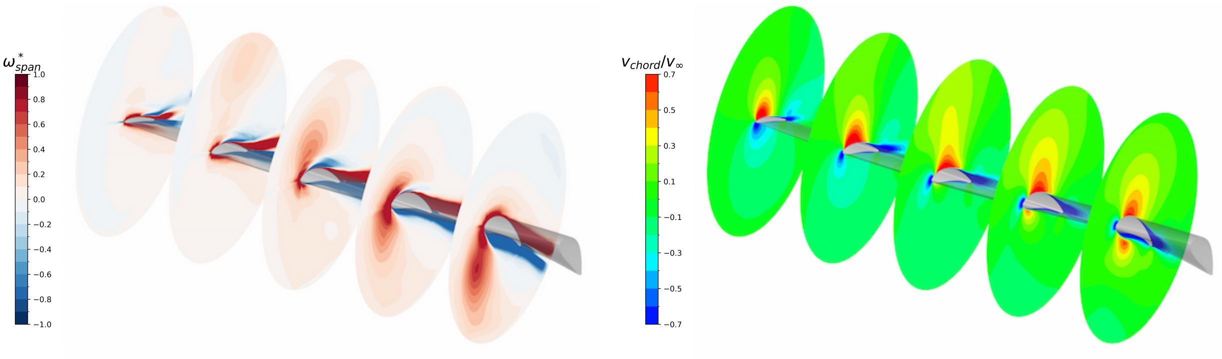

(a) non-dimensional spanwise vorticity (b) normalized chordwise relative velocity

Figure 22: Rear propeller: BVI when blade exits overlapping region at $\psi = 245^\circ$ for case CW-CCW_60 at $J = 0.8$

Aerodynamics," *Journal of Aircraft*, Vol. 60, (2), 2023, pp. 521–532. DOI: 10.2514/1.C036808.

13. Yang, Y., Xu, G., Shi, Y., and Hu, Z., "Analysis of the Aeroacoustic Characteristics of a Rigid Coaxial Rotor in Forward Flight Based on the CFD/VVPM Hybrid Method," *Aerospace*, Vol. 11, (1), January 2024, pp. 21. DOI: 10.3390/aerospace11010021.

14. Yuan, Y., and Vigevano, L., "Assessment of a Hybrid Eulerian-Lagrangian Method by Comparison with Its Parent Codes," 50th European Rotorcraft Forum (ERF 2024), 2024.

15. Biava, M., and Vigevano, L., "Simulation of a Complete Helicopter: A CFD Approach to the Study of Interference Effects," *Aerospace Science and Technology*, Vol. 19, (1), June 2012, pp. 37–49. DOI: 10.1016/j.ast.2011.08.006.

16. Tugnoli, M., Montagnani, D., Syal, M., Droandi, G., and Zanotti, A., "Mid-Fidelity Approach to Aerodynamic Simulations of Unconventional VTOL Aircraft Configurations," *Aerospace Science and Technology*, Vol. 115, August 2021, pp. 106804. DOI: 10.1016/j.ast.2021.106804.

17. Spalart, P. R., and Allmaras, S. R., "A One-Equation Turbulence Model for Aerodynamic Flows," 30th AIAA Aerospace Science Meeting & Exhibit., 1992. DOI: 10.2514/6.1992-439.

18. Roe, P. L., "Approximate Riemann Solvers, Parameter Vectors, and Difference Schemes," *Journal of Computational Physics*, Vol. 135, (2), August 1997, pp. 250–258. DOI: 10.1006/jcph.1997.5705.

19. Jameson, A., "Time Dependent Calculations Using Multigrid, with Applications to Unsteady Flows Past Airfoils and Wings," 10th Computational Fluid Dynamics Conference, 1991. DOI: 10.2514/6.1991-1596.

20. Cottet, G.-H., and Koumoutsakos, P. D., *Vortex Methods: Theory and Practice*, Cambridge University Press, Cambridge ; New York, 2000.

21. Zanotti, A., Velo, A., Pepe, C., Savino, A., Grassi, D., and Riccobene, L., "Aerodynamic Interaction Between Tandem Propellers in eVTOL Transition Flight Configurations," *Aerospace Science and Technology*, Vol. 147, April 2024, pp. 109017. DOI: 10.1016/j.ast.2024.109017.

22. Kim, J. W., and Lee, D. J., "Generalized Characteristic Boundary Conditions for Computational Aeroacoustics," *AIAA Journal*, Vol. 38, (11), November 2000, pp. 2040–2049. DOI: 10.2514/2.891.

23. Johnson, W., and Silva, C., "NASA Concept Vehicles and the Engineering of Advanced Air Mobility Aircraft," *The Aeronautical Journal*, Vol. 126, (1295), January 2022, pp. 59–91. DOI: 10.1017/aer.2021.92.

24. Johnson, W., Silva, C., and Solis, E., "Concept Vehicles for VTOL Air Taxi Operations," AHS Specialists "Conference on Aeromechanics Design for Transformative Vertical Flight., 2018.

25. Chakraborty, I., and Mishra, A. A., "Sizing and Analysis of a Lift-Plus-Cruise Aircraft with Electrified Propulsion," *Journal of Aircraft*, Vol. 60, (3), May 2023, pp. 747–765. DOI: 10.2514/1.C037044.

26. Caccia, F., Abergo, L., Savino, A., Morelli, M., Zhou, B. Y., Gori, G., Zanotti, A., Gibertini, G., Vigevano, L., and Guardone, A., "Multi-Fidelity Numerical Approach to Aeroacoustics of Tandem Propellers in eVTOL Airplane Mode," AIAA AVIATION 2023 Forum, June 2023. DOI: 10.2514/6.2023-3221.

CLASSIFICATION & COPYRIGHT

as ERF proceedings. In addition, they will be available in a freely accessible web-based repository 2 years after the respective conference.